


## Microscopic origin of shear banding as a localized driven glass transition in compressed colloidal pillars

Daniel J. Strickland,<sup>1</sup> Drew S. Melchert,<sup>2</sup> Jyo Lyn Hor,<sup>1</sup> Carlos P. Ortiz,<sup>1</sup> Daeyeon Lee,<sup>1</sup> and Daniel S. Gianola<sup>2,\*</sup>

<sup>1</sup>University of Pennsylvania, Philadelphia, Pennsylvania 19104, USA

<sup>2</sup>University of California Santa Barbara, Santa Barbara, California 93106, USA

 (Received 5 February 2020; revised 20 July 2020; accepted 21 July 2020; published 8 September 2020)

Here we report on compression experiments of colloidal pillars in which the evolution of a shear band can be followed at the particle level during deformation. Quasistatic deformation results in dilation and anisotropic changes in coordination in a localized band of material. Additionally, a transition from solid- to liquidlike mechanical response accompanies the structural change in the band, as evidenced by saturation of the packing fraction at the glass transition point, a diminishing ability to host anelastic strains, and a rapid decay in the long-range strain correlations. Overall, our results suggest that shear banding quantitatively resembles a localized, driven glass transition.

DOI: [10.1103/PhysRevE.102.032605](https://doi.org/10.1103/PhysRevE.102.032605)

### I. INTRODUCTION

Shear banding—the irreversible localization of strain in thin bands of a solid driven beyond its yield stress—is a feature common to disordered solids. Shear bands are observed in both “hard” disordered solids, where atomic forces dictate the energy of the system [1,2], and in “soft” disordered solids, whose behavior is governed by weaker interparticle forces [3–5]. Also common to both hard and soft disordered solids is a glass transition, whereby decreasing the temperature, increasing the particle number density, or some combination thereof results in a dramatic slowing of the dynamics in comparison to the supercooled liquid [6–9]. The commonalities in plasticity and glassy dynamics found in a diverse set of disordered solids have motivated a search for unifying physics. Specifically, the interpretation of shear banding as a localized, driven glass transition remains controversial.

Numerical and experimental studies support a connection between mechanical yield and the glass transition. Metallic glasses (MGs) exhibit shear bands and a temperature-dependent yield stress when deformed plastically at temperatures well below their glass transition temperature  $T_g$  [1,2,10]. Equating the mechanical work done in the formation of a shear band and the heat necessary to induce a glass transition [11] results in a scaling of the yield strength with temperature that agrees well with experimental data. Further support for a shear band-glass transition connection is found in the self-similarity of isoviscosity curves with proximity to the glass transition and magnitude of applied stress [12–15], which is suggestive of an equivalence between the glass transition and stress required for flow. However, the studies in Refs. [12–14] do not specify whether plasticity is spatially homogeneous or localized in shear bands, while other studies draw a distinction between shear banding and the glass transition. In experiments

on a sheared colloidal glass, Chikkadi *et al.* [16] find a discontinuity in a dynamical order parameter that distinguishes shear banding from a glass transition, in which the order parameter changes continuously [6]. Similarly, a structural order parameter that segregates pre- and postyield glasses classifies mechanical yield as a first-order transition [17]. Others have delineated between the glass transition and mechanical yield by contrasting the microstates induced by strain and increased temperature [18] and anisotropy of dynamical correlations [19], which are different for the thermal and mechanical transitions.

While it appears that mechanical yielding in disordered solids shares some characteristics with the glass transition, the extent of the correlation is not agreed on. The microscopic details of shear bands as they mature to macroscopic localization have yet to be elucidated. In this article, we report on uniaxial compression experiments of colloidal pillars. Unlike other studies on deformed colloidal glasses, our specimens are free of confining boundaries that may alter the mechanism by which shear banding proceeds [3,4,16,20]. Moreover, the pillar geometry lends itself directly to comparison with compression experiments performed on MGs [21,22]. In the unconfined geometry, dilation is free to occur and any localized softening can proceed unhindered.

During compression, we observe strong localization of strain in a band of the pillar. As deformation proceeds, the sheared region continues to dilate until the packing fraction  $\phi$  approaches the colloidal glass transition,  $\phi_g \simeq 0.58$  [23], at which point dilation terminates. While the transition in mechanical response bears some resemblance to a melting condition in thermal, atomic systems, we emphasize that our system of colloidal spheres is athermal. We quantify the extent of correlations in strain and find that it decreases as  $\phi \rightarrow \phi_g$  and find evidence of a diminished capability to support anelastic strain from anisotropic pair distribution functions (PDFs).

\*Corresponding author: [gianola@ucsb.edu](mailto:gianola@ucsb.edu)

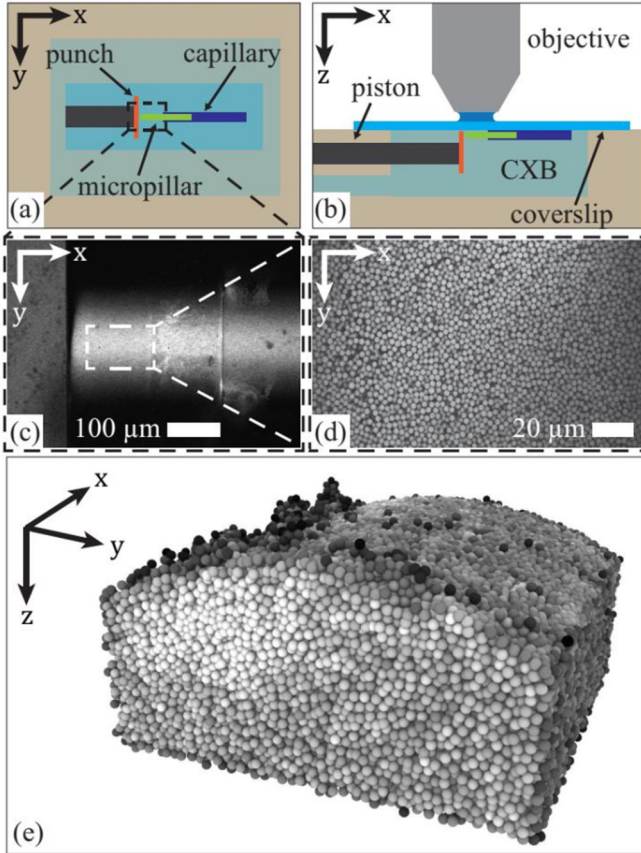


FIG. 1. A (a) top-down and (b) side view of the experimental setup. The capillary tube containing the colloidal micropillar is secured to a glass coverslip, which is fixed above a fluid reservoir. A piston with a flat punch is used to compress the exposed micropillar. (c) A low-magnification image of an extruded micropillar and the punch. (d) A high-magnification image of the colloidal particles that compose the micropillar. (e) A three-dimensional reconstruction of the pillar section imaged during the experiments using the identified particle positions. The particles are shaded by coordination number, highlighting the curved free surface.

## II. EXPERIMENTAL DETAILS

The micropillars, of diameter  $D_{\text{pillar}} \approx 300 \mu\text{m}$ , are composed of fluorescent poly(methyl methacrylate) (PMMA) particles of diameter  $D_{\text{part}} = 3.3 \mu\text{m}$ . The micropillars are formed by injecting a suspension of the particles into a capillary tube. Polydispersity of between 6 and 8% in the particle sizes suppresses crystallization, resulting in an amorphous packing. The suspension is dried and rewetted using cyclohexylbromide (CXB, which matches the index of refraction of the particles) to increase the cohesion between the particles, holding the extruded specimen together. The pillar is then forced out of the capillary tube to form a free-standing compression specimen, which is secured in a fluid reservoir filled with CXB (see Fig. 1), eliminating capillary forces. Opposing the pillar is a punch affixed to a piston. The top of the reservoir is sealed with a thin piece of coverglass to allow for imaging using a laser-scanning confocal microscope operating in fluorescence mode with an excitation wavelength of 488 nm. The

compression experiment proceeds by displacing the punch using a piezoelectric actuator and then collecting a sequence of micrographs of the pillar. Typical displacement increments were  $0.6 \mu\text{m}$  ( $\sim 0.2D_{\text{part}}$ ). A computer algorithm identifies the centers of particles in each three-dimensional (3D) volume with uncertainty in the particle positions of  $\sim 0.03D_{\text{part}}$ . The analysis proceeds by the same stages as the classic algorithm by Grier and Crocker [24]: image filtering, peak finding, and centroid finding. This process and an uncertainty analysis are detailed in Appendices A and B. After particle centers are identified, the positions at each time step are linked into trajectories that span the duration of the compression experiment. Particles within three particle diameters of the punch are removed from the analysis, since shadowing during imaging resulted in high uncertainty in their positions.

## III. RESULTS AND DISCUSSION

### A. Volume fraction

During compression, we observe strain concentrated in a region near the interface with the punch. The shear band is defined here as those particles with shear strain  $\gamma > 0.07$  (calculated from the affine deformation tensor as detailed in Eq. (2)) that have at least three neighbors which also satisfy this strain threshold. This neighbor condition filters out non-contiguous particles. The effect of adjusting the parameters used in this definition is shown in Fig. 2: the local volume fraction in the as-defined shear band shows little sensitivity to the shear strain threshold or neighbor filtering except at the first time steps when the number of particles in the shear band is small. Those particles not in the shear band are termed “the matrix.” A time step  $t$  refers to a specific 3D volume with  $t = 0$  corresponding to the first volume collected.

The initial packing fraction and Voronoi volume distribution indicate that the shear band was somewhat deformed before the first time step, so that nascent nucleation of the shear band is not captured in this experiment. However, we are able to observe the evolution of this already-nucleated shear band as deformation proceeds [Fig. 3(b)] and find, based on a number of metrics, that its maturation shows a striking resemblance to a localized, shear-driven colloidal glass transition. The first metric is the local packing fraction: the shear band region dilates such that the volume fraction  $\phi = 4\pi r^3 / (3\bar{V}_{\text{Voronoi}})$ , where  $\bar{V}_{\text{Voronoi}}$  is the mean of the Voronoi volumes of the particles in the shear band, decreases to approximately the colloidal glass transition value  $\phi_g \approx 0.58$  [Fig. 3(c)]. We expect our nearly athermal system to be in a glassy state between  $0.58 < \phi < 0.64$ , below which it fluidizes and above which it is jammed [25]. We note that the exact value of  $\phi_g$  for hard-sphere colloids remains uncertain and may depend on the polydispersity of the system [23,26,27], and thus the saturation point (where further compression does not significantly change  $\phi$ ) is either at the transition or in the supercooled colloidal liquid [28,29]. Dilution is also visible in the evolution of the distribution of Voronoi volumes  $P(V_{\text{Voronoi}})$  [Figs. 3(d) and 3(e)], which shifts to a higher mean value and develops a large-volume tail. The matrix, on the other hand, has constant  $\phi$  near the random

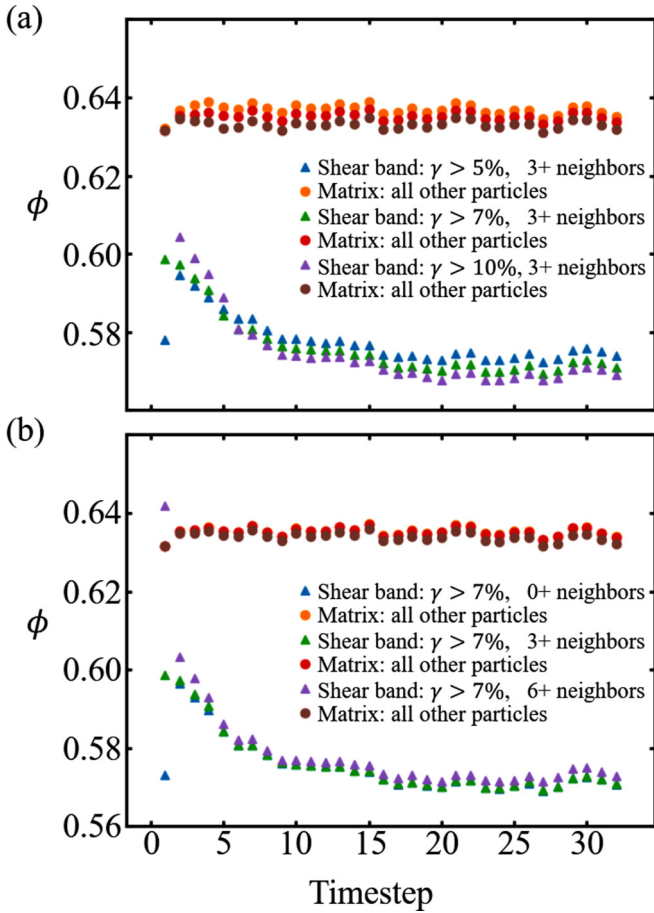


FIG. 2. Saturation behavior of the volume fraction  $\phi$  in the shear band and matrix using various parameter cutoffs in the shear band definition: (a) variation of the cutoff in shear strain  $\gamma$  and (b) variation of the requisite number of nearest neighbors which also meet the shear strain condition, which serves to filter out noncontiguous sheared particles.  $\phi$  shows little sensitivity to these parameters in this range, except at the first time step where there are few particles in the shear band.

close-packing limit of 0.64 (indicating that our particles have RMS roughness  $< 0.05$  [30]).

It has long been recognized that shear transformations in amorphous solids result in an increase in the free volume in the region around the shear transformation [31–34]. In thermal systems, the competition between shear-induced generation and diffusion-driven annihilation of free volume results in temperature- and strain rate-dependent flow behavior [35–37]. At high temperatures and low strain rates, free volume diffusion and annihilation can suppress runaway free volume generation, resulting in homogeneous plastic flow. At lower temperatures and high strain rates, annihilation cannot keep up with free volume generation, and strain localization, or heterogeneous plastic flow, occurs. For our nearly athermal, hard-sphere system, we expect that the annihilation of excess free volume is insignificant in comparison to the shear-driven generation, thereby resulting in overall dilation with increasing strain [33]. What is striking, however, is how abruptly

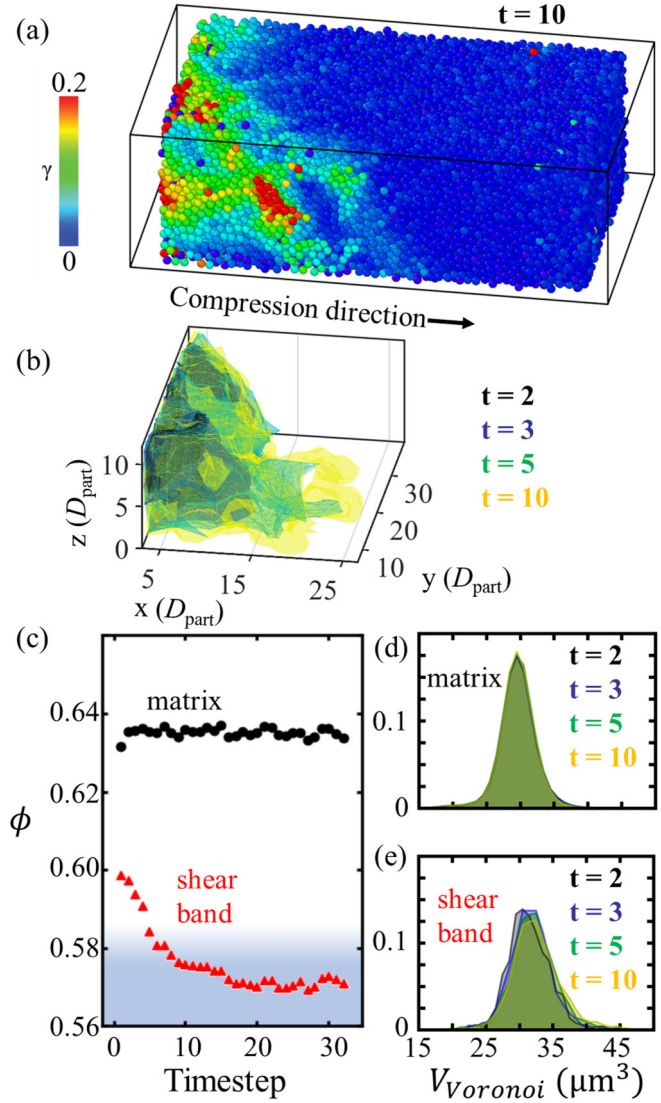


FIG. 3. (a) The particles in this experiment, colored by shear strain. The shear band is defined as those particles with  $\gamma > 0.07$  which have at least three neighbors also with  $\gamma > 0.07$ . (b) The evolution of the shear band shape over time, visualized as the alpha shape with the smallest alpha radius which encloses all particles in the shear band. (c) The volume fraction  $\phi$  of the shear band and matrix regions, with glass transition indicated with a blue shaded region. [(d) and (e)] The distribution of Voronoi volumes in the shear band and matrix at various time steps.

the dilation process in our experiments terminates at the transition  $\phi_g$ .

### B. Pair distribution function

The dilation and Voronoi statistics measured in the shear band clearly indicate that the structure in the shear band is evolving during deformation. To further describe this change, anisotropic pair distribution functions that discriminate between particle pairs coordinated in different directions,  $g(\mathbf{r}) = g(r, \omega)$ , where  $\omega$  is the angle between the loading axis and a selected direction, detect structural changes when symmetry

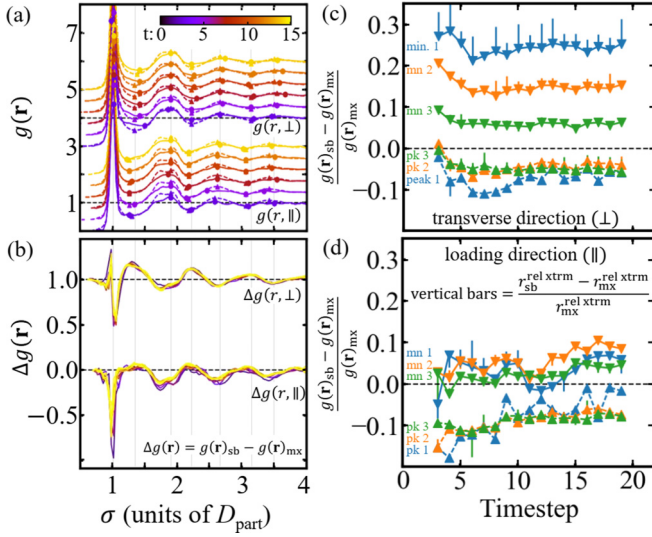


FIG. 4. (a) Pair distribution function plots measured for the shear band particles (solid lines) and matrix particles (dashed lines), along the parallel and perpendicular directions to the loading. Local minima and maxima, calculated using a polynomial fit, are indicated with markers. Curves are offset for clarity. (b) Plots of the difference in  $g(\mathbf{r})$  between shear band and matrix for each direction. (c) Fractional peak height differences between shear band and matrix for the transverse and (d) loading directions. Peak shifts are indicated by the vertical bars, where a positive (upward) bar indicates a shift to greater  $r$  in the shear band relative to the matrix.

is broken by anisotropic loading [38,39]:

$$g(r, \omega) = \frac{1}{f(r, \omega)} \frac{V}{N^2 dV} 2 \sum_{i=0}^{N-1} \sum_{j>i}^N \delta\left(r - \frac{dr}{2} < r_{ij} < r + \frac{dr}{2}\right) \times \delta\left(\omega - \frac{d\omega}{2} < \omega_{ij} < \omega + \frac{d\omega}{2}\right), \quad (1)$$

where  $V$  is the total volume and  $N$  is the number of particles in the shear band,  $dV = 2r^2 dr d\omega$  is the volume element of a spherical shell (at  $r$  and with thickness  $dr$ ) constrained by azimuthal angle  $\omega$  between the  $x$  axis and the vector separating a given  $i, j$  pair (always positive), and  $\delta$  is the Kronecker delta. Here  $dr = 0.04D_{\text{part}}$  and  $d\omega = \pi/10$ .  $f(r, \omega)$  is the shape factor that normalizes the pair distribution function for a finite sample volume, calculated as the pair density for the continuum bounded by the shear band (i.e., points spaced apart by a distance  $r \ll D_{\text{part}}$  divided by the pair density for an unbounded, infinite sample. This shear band volume is calculated as the union of all shear band particle Voronoi volumes.

Examining the pair distribution functions along the loading axis and the perpendicular direction,  $g(r, \parallel) = g(r, \omega = 0)$  and  $g(r, \perp) = g(r, \omega = \pi/2)$ , respectively, we identify peaks in  $g(\mathbf{r})$ , which mark the location of the nearest-neighbor shells, as well as local minima [Fig. 4(a)]. In both directions, peak heights in  $g(\mathbf{r})$  decrease in the shear band (relative to the matrix particles at the same time step), while the relative minima increase. This peak broadening indicates a less structured packing. The split second peak in the matrix, which reflects local icosahedral order [40], is also absent in the shear band, particularly at later time steps and along the loading direction.

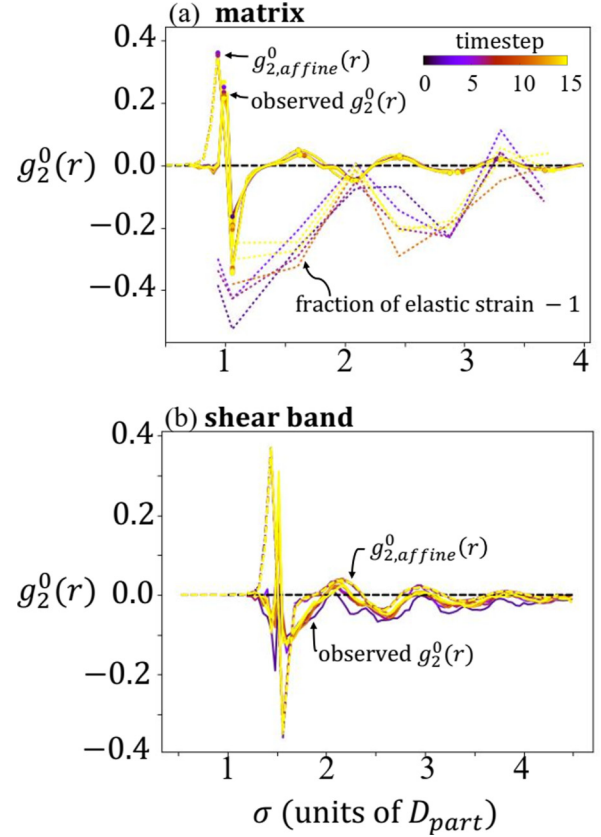


FIG. 5. The anisotropic PDF decomposed by spherical harmonics. (a) In the unsheared matrix particles, the peaks of  $g_{2,\text{affine}}^0(r)$ , are fit to the observed  $g_2^0(r)$ , giving the fraction of the observed strain relative to the elastic (applied) strain  $\epsilon$  [38,42,43]. This fraction is plotted and offset by 1, for ease of viewing. (b) In the shear band, such a fit is not possible, since the observed  $g_2^0(r)$  does not deviate symmetrically from the affine curve. The first time step plotted here,  $t = 4$ , is subject to sampling errors in the normalization since the particle number is small in the shear band at early time steps.

The  $g(\mathbf{r})$  difference plots in Fig. 4(b) shows in more detail that the magnitude of the peaks in  $g(\mathbf{r})$  decreases in the loading direction significantly more than in the transverse direction, while the intensity at the minima in  $g(\mathbf{r})$  increases more in the transverse directions. This indicates that nearest-neighbor “bonds” are broken primarily along the loading direction, and particles move to the spaces between nearest-neighbor shells in the transverse direction. See Suzuki *et al.* 1987 [39] for schematic illustrations of such rearrangements. Based on percentage changes in peak heights [Figs. 4(c) and 4(d)] the nearest-neighbor shell within the shear band is  $\sim 10\%$  less populated in the loading direction compared to the matrix, while in the transverse direction the first local minimum (the space between the first two shells) is more populated by  $>20\%$ , and the second minimum is  $\sim 15\%$  more populated. The higher- $r$  local extrema (at  $r > 4D_{\text{part}}$ ) have  $<6\%$  change.

These changes in  $g(\mathbf{r})$  suggest that the presence of anelastic strain in the shear band which serves to screen the imposed stress manifest as particle rearrangements from the loading direction to the transverse direction. This mechanism has been observed in x-ray scattering experiments on metallic glasses,

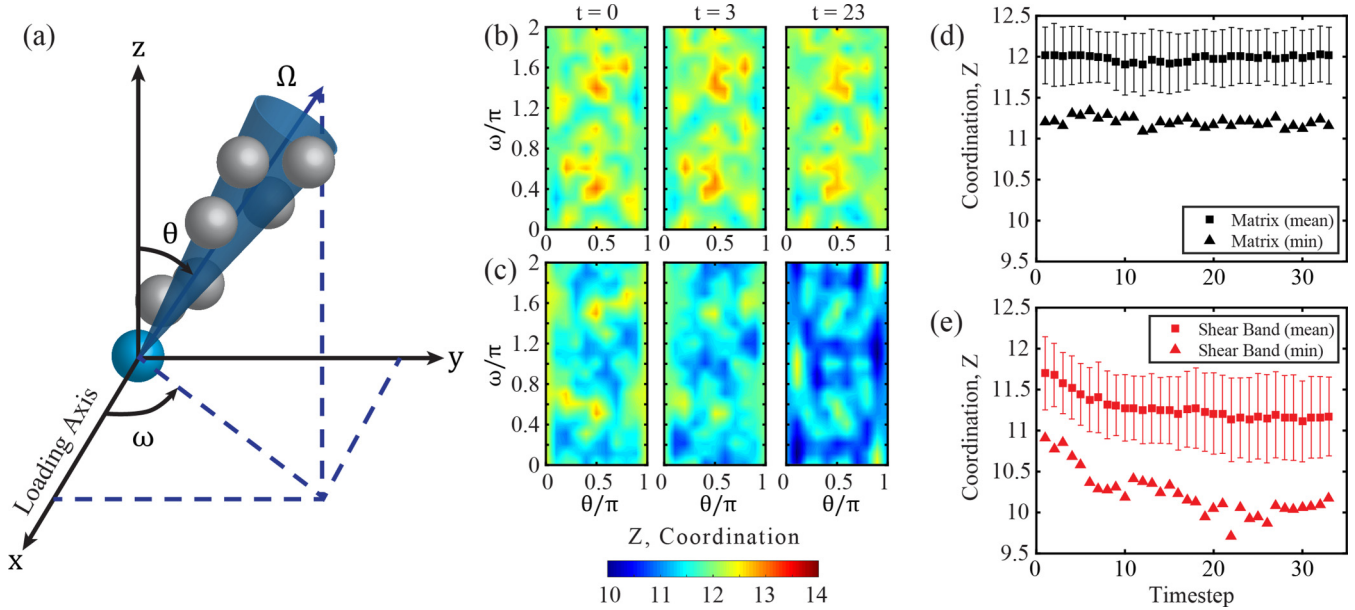


FIG. 6. (a) The spherical coordinate conventions used to determine the average coordination along a given direction. Note that the azimuthal angle  $\omega$  is used as an elevation angle in the pair distribution definition function above. The angular coordination in the matrix, row (b), and the shear band, row (c), at three time steps. Little change in the coordination is observed in the matrix. The shear band, however, shows a decrease in the mean coordination and a decrease in the anisotropy of the coordination. The changes in  $Z$  in the matrix and shear band (here defined generously as a rectangular region) are quantified in (d) and (e), respectively, which show the evolution of the mean and minimum of  $Z$  with time step. The error bars represent the standard deviation in  $Z$ .

as well as in molecular dynamics simulations on similar systems [38,41,42]. The peak height differences in the parallel direction and local minimum differences in the transverse direction decrease in magnitude and reach a stable value by  $t = 10$  (i.e., during dilation), indicating a diminished capacity to support anelastic strains, as expected in a fluidized region. The short-range spatial extent of rearrangements (i.e., vanishing differences in  $g(\mathbf{r})$  for  $r > 4D_{\text{part}}$ ) is in good agreement with studies on crept metallic glasses and molecular dynamics glass models, which observe a cutoff in local (anelastic) strains at  $r = 4D_{\text{part}}$  [38,43].

To quantify this anelastic activity, we also compare  $g_2^0(r)$ , the  $l = 2$  spherical harmonic of the anisotropic PDF, to the values expected to arise from affine deformation, where  $g_2^0(r) \propto g(r_{\parallel}) - g(r_{\perp})$  and  $g_{2,\text{affine}}^0(r) \propto \epsilon r \frac{dg_0(r)}{dr}$  [39]. As shown in Fig. 5, in the matrix this reveals short-range anelastic strains like those seen in MGs, which screen 20–40% of the elastic strain for  $r$  under  $2 - 4D_{\text{part}}$  [38,42,43]. In the shear band, however, the observed  $g_2^0(r)$  does not deviate symmetrically from the affine (elastic) assumption  $g_{2,\text{affine}}^0(r)$ , indicating that the shear band does not support elastic strain but preventing quantification of anelastic strain.

### C. Directional coordination

Another detailed measure of the local structure is the directional coordination, which can be extracted from  $g(\mathbf{r})$ . A cone with its axis along a direction vector (with azimuthal angle  $\omega$  and elevation angle  $\theta$ ) is defined so that the solid angle of the cone is given by  $\Omega$ . Note that the azimuthal angle  $\omega$  is used as an elevation angle in the pair distribution function definition above. All points within the cone are selected, and then the

directionally dependent coordination  $Z(\theta, \omega) = \int_0^{r_{\min}} \eta g(\mathbf{r}) d\mathbf{r}$  is calculated, where  $r_{\min}$  is the value of  $r$  at the first minimum in  $g(r)$  and  $\eta$  is the particle number density  $N/V$ .

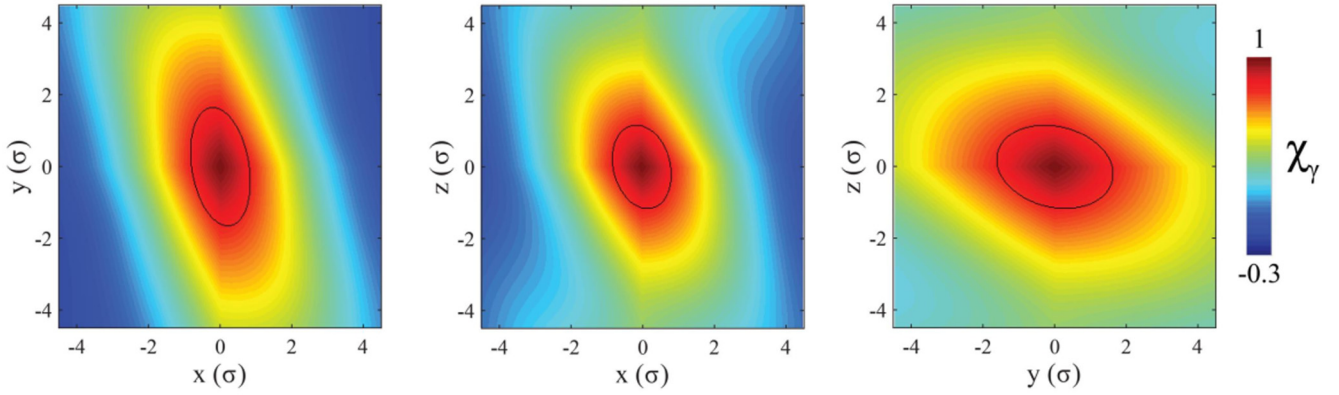
Figures 6(b) and 6(c) show the angular coordination in the matrix and shear band, respectively, at three time steps. It is apparent that the shear band, which was preformed at  $t = 0$ , is on average undercoordinated with respect to the matrix, with particular undercoordination along  $\{\theta \approx \pi/2, \omega \approx \pi\}$  [see Figs. 6(d) and 6(e)]. As deformation proceeds,  $Z$  in the shear band continues to decrease and becomes more anisotropic, which is reflected in the increasing standard deviation in  $Z$  [Fig. 6(e)], with the most undercoordinated directions finally lying along  $\{\theta \approx \pi, \omega \approx \pi\}$  and  $\{\theta \approx 0, \omega \approx 0\}$ . The closest-packed directions are along  $\{\theta \approx \pi/4, \omega \approx \pi/2\}$  and  $\{\theta \approx 3\pi/4, \omega \approx 3\pi/2\}$ , which correspond to directions of minimum (deviatoric) shear for the uniaxial compression geometry. This result is in contrast to previous studies, which find more coordination along directions of high shear [44].

In stark contrast,  $Z$  in the matrix shows little change in both the mean and minimum coordination [see Fig. 6(d)]. On average, the shear band lacks one neighbor in comparison to the matrix, with the most undercoordinated directions having only  $\sim 10$  neighbors in comparison to the matrix's mean value of 12. The evolution of  $Z$  in the shear band shows the same behavior as  $\phi$  in that it remains static after  $t = 10$ .

### D. Strain correlation function

These structural signatures collectively point to a solid-to liquidlike transition wherein the shear band prior to the transition can sustain elastic stress due to anelastic

## (a) shear band



## (b) matrix

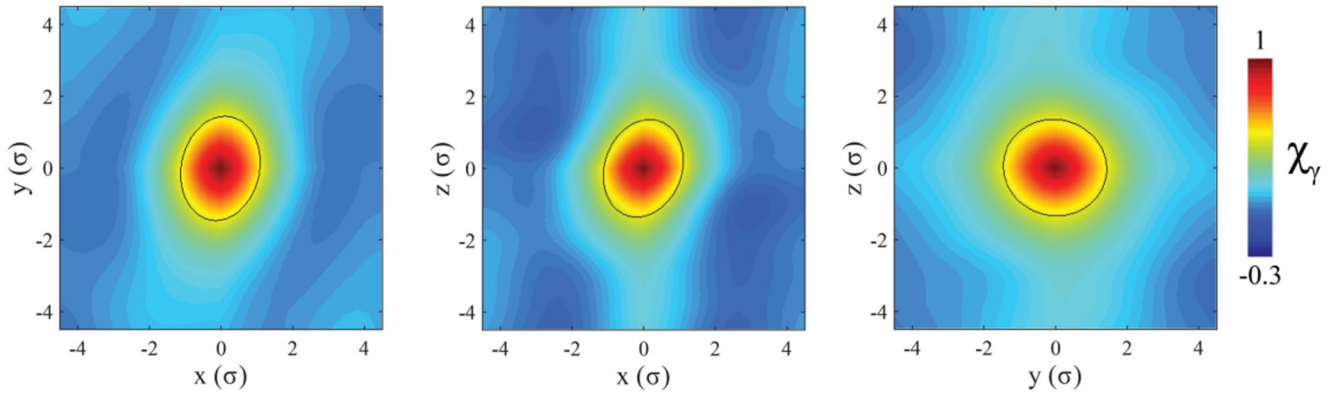


FIG. 7. Slices along the  $x$ - $y$ ,  $x$ - $z$ , and  $y$ - $z$  planes of the strain correlation functions in both the (a) shear band and (b) the matrix. An ellipsoid is fit to an isointensity surface of the 3D correlation. The anisotropy of the ellipsoid is quantified by the ratio of the major axis length to the minor axis length.

rearrangements, whereas after the transition the rearrangements in the shear band become fully plastic to relax the internal stresses. In metallic glasses, it has been shown that structural rejuvenation via thermal or mechanical processing can increase the material's capacity for plastic strain prior to catastrophic failure [45,46]. Our measurements of structural change directly in the shear band of a colloidal glass suggest an upper bound to the extent of rejuvenation possible in a finite volume of material. To establish a link between structure and local mechanical response, we analyze the spatial extent of local shear deformation as measured by the shear strain correlation function  $\chi_\gamma$ , calculated as follows.

We find the best affine deformation tensor  $\mathbf{J}_k$  for particle  $k$  that maps particle  $k$ 's neighbors at time  $t$  to their positions at time  $t + \Delta t$  by minimizing the total nonaffine displacement  $D_{\min,k}^2 = 1/N \sum_{i=1}^N [ \mathbf{r}_i(t + \Delta t) - \mathbf{J}_k \mathbf{r}_i(t) ]^2$  [47]. A cut-off distance of  $2D_{\text{part}}$  to identify a particle's neighbors was employed. The strain tensor  $\boldsymbol{\epsilon}_k$  is found by extracting the symmetric part of  $\mathbf{J}_k$  as  $\boldsymbol{\epsilon}_k = \frac{1}{2}[\mathbf{J}_k + \mathbf{J}_k^T]$ , which allows for the calculation of the shear strain  $\gamma_k = \sqrt{\frac{1}{2} \text{Tr}(\boldsymbol{\epsilon}_k - \Delta_k \mathbf{I})}$ , where  $\Delta_k = \frac{1}{3} \text{Tr}(\boldsymbol{\epsilon}_k)$  is the hydrostatic strain invariant. At each time

step, the spatial autocorrelation of  $\gamma(\mathbf{r})$  is computed as:

$$\chi_\gamma(\mathbf{dr}) = \frac{\langle \gamma(\mathbf{r})\gamma(\mathbf{r} + \mathbf{dr}) \rangle - \langle \gamma(\mathbf{r}) \rangle^2}{\langle \gamma(\mathbf{r})^2 \rangle - \langle \gamma(\mathbf{r}) \rangle^2}. \quad (2)$$

$\chi_\gamma$  is found to be quite anisotropic, but generally ellipsoidal, as shown in Fig. 7, with particular directions exhibiting strong correlation at large distances, as expected in shear-dominated dynamics [48]. To quantify changes in the correlations as deformation proceeds, an ellipsoid is fit to an isointensity surface for each  $\chi_\gamma(\mathbf{dr})$ . The value of  $\chi_\gamma$  as a function of distance  $\sigma = r/D_{\text{part}}$  along the ellipsoid's major axis is a measure of the maximum extent of the correlation in strain and is plotted in Figs. 8(a) and 8(b). At each time step, we fit  $\chi_\gamma$  to an exponential form  $\chi_\gamma = \exp(-\sigma/\zeta)$  to extract the correlation length  $\zeta$ , an approximate measure of rearrangement size [49].

These correlation lengths are plotted against the local volume fraction  $\phi$  at the corresponding time step in Fig. 8(c). In the matrix, the correlations are relatively unchanged throughout the experiment, with zero correlation beyond  $\sigma = 4$ , suggestive of minimal plastic activity and a shedding of any

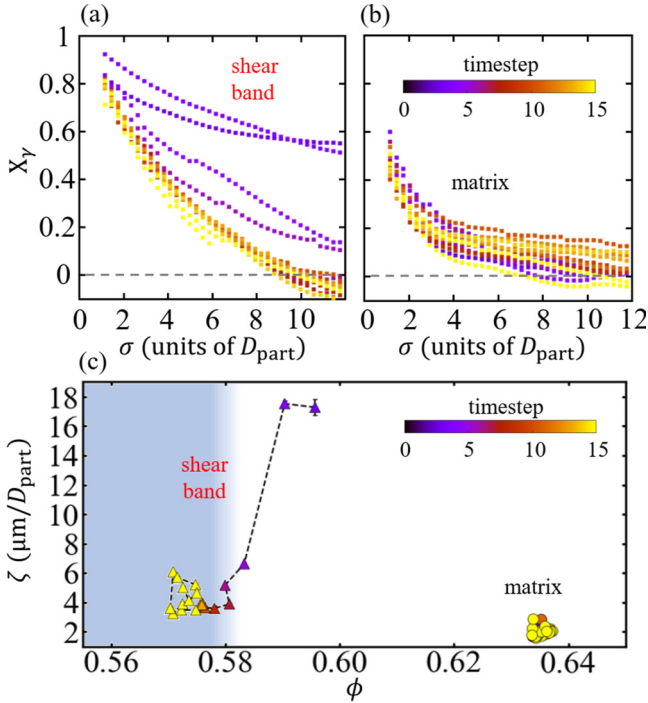


FIG. 8. (a) Decay of the strain correlation  $\chi_y$  along the major ellipsoidal axis in the shear band and (b) matrix at different time steps. (c) The correlation lengths  $\zeta$  from a fit to exponential decay  $\chi_y = \exp(-\sigma/\zeta)$  plotted versus volume fraction  $\phi$ . Data points for  $t \geq 15$  [not shown in (a) and (b)] have the same coloring. Error bars mark the standard deviation of the errors of the fit, obscured by plot markers in most cases.

elastic stresses in favor of localized plastic deformation in the shear band. In the shear band, the spatial extent of the correlations decays as deformation proceeds. At  $\phi > \phi_g$ , the correlation at  $\sigma = 10$  is significant with  $\chi_y(\sigma = 10) \approx 0.2-0.6$ , and correlation lengths are high, indicative of cooperative rearrangements system-spanning shear band, as has been observed in glass models at the yielding point [50]. Further dilation, however, reduces  $\zeta$ . Notably, the time step where  $\zeta$  reaches a minimum corresponds to the same time step,  $t = 10$ , where both  $\phi$  and  $Z$  sharply saturate. This decay in the correlation lengths in shear strain signifies a transition from a solidlike to liquidlike response, which accompanies the changing structure within the shear band [50,51]. We also find that the anisotropy of the correlation, quantified by the ratio of the ellipsoid's major to minor axis, decays with dilation in the shear band from  $\sim 3$  to  $\sim 1.5$  (see Fig. 7). The correlation in the matrix is isotropic, with anisotropy values  $\sim 1.1$  that persist throughout the experiment. We note that while the correlation lengths of the developing shear band tend to those of the matrix [Fig. 8(c)], they reflect different physics, as evident in the full dependence of the strain correlations with distance [Figs. 8(a) and 8(b)]. In the shear band, the long-range correlation in strain at early time steps is reminiscent of perfect slip along two planes. As the band fluidizes at later time steps, the correlation length between plastic events decays to  $\sim 5D_{\text{part}}$ . In contrast, the matrix remains relatively undeformed once the shear band forms and only isolated

plastic rearrangements occur in a manner that is relatively insensitive to the progression of the experiment, as has been observed in quiescent and deformed colloidal solids [52]. These results show the structural and mechanical transitions, as measured by  $\phi$ ,  $g(r, \omega)$ , and  $\chi_y$ , to be quite abrupt and consistent with a short-range transition in structure.

#### IV. CONCLUSION

Overall, our results quantitatively support the interpretation of shear banding as a driven, localized glass transition. Quasistatic deformation drives a reduction in  $\phi$  in a thin band of the solid until  $\phi$  approaches  $\phi_g$ , at which point there is a sharp transition and dilation ceases. Dilation is accompanied by a decay in the extent and anisotropy of spatial correlations in strain as well as a diminished capacity to support anelastic strains, which would give rise to memory effects before the onset of full plasticity, signifying a transition from solidlike to liquidlike response [33]. While we cannot rule out a first-order transition in the particle dynamics, the observed continuous changes in structure and mechanical response are consistent with the behavior of a glass as it approaches the glass transition from the solid phase. By definition, the spatial extent of the changes in structure and response is heterogeneous, and the resulting microstructure is clearly distinct from a microstructure that may be obtained from isotropic dilation, which is consistent with the conclusions drawn in Refs. [18,19]. Our results providing the microscopic origins of such driven transitions lend credence to an equivalency between mechanical shear banding and the glass transition provided that careful consideration of the spatial extent of the system is given.

#### ACKNOWLEDGMENTS

We acknowledge financial support from the National Science Foundation through University of Pennsylvania Materials Research Science and Engineering Center DMR-1120901. D.S.G. acknowledges partial support from the NSF MRSEC Program through DMR 1720256 (IRG-1). We also thank A. Liu, D. J. Durian, and Robert Ivancic for insightful discussions.

#### APPENDIX A: CONFOCAL MICROGRAPH ANALYSIS

##### 1. Image filtering

Since our samples are polydisperse, we filter the original images with a three-dimensional, scale-free Laplacian of Gaussian kernel,  $L(x, y, z)$ . The filter operation is implemented as a convolution operation  $I = I * L$ , computed by the fft method along each dimension [53]. This kernel is given explicitly as:

$$L(x, y, z) = \frac{1}{A} (x^2/\sigma_x^2 + y^2/\sigma_y^2 + z^2/\sigma_z^2 - 3) \times \exp[-(x^2/\sigma_x^2 + y^2/\sigma_y^2 + z^2/\sigma_z^2)/2], \quad (\text{A1})$$

where the normalization constant is  $A = 2\sqrt{2}\pi^{3/2}\sigma_x\sigma_y\sigma_z$ . This functional form of  $L(x, y, z)$  was originally suggested by Lindeberg [54]. Lindeberg showed that it is necessary to normalize Laplacian operators by  $\sigma^2$  in order to remove

the systematic dependence of the Laplacian operator on the probing size, enabling the comparison of the response of objects of different sizes on even terms. This allows the signal of small particles near large particles to be recovered without doing a prohibitively slow multisize search algorithm, with polydispersities even as large as a few hundred percentages. Here the kernel widths  $\sigma_i$  are chosen such that the full-width half-max of the kernel equals the mean particle size in pixels along each dimension,  $\sigma_i = R_i/\sqrt{2\ln(2)}$ .

## 2. Peak finding

The peak find algorithm is identical in outline to the original implementation by Grier and Crocker. Our implementation seeks to vectorize and memory manage the operations to optimize the analysis of three-dimensional image stacks. For each voxel, we compare its intensity to every neighbor in a  $3\times 3\times 3$  region. This operation is vectorized to the number of voxels that can be simultaneously held in memory. For each local region, we use grayscale dilation and erosion operations to identify the locations of local maximum and local minimum intensities and test whether the center voxel coincides with either. Voxels that align with regional maxima in intensity are kept as candidate centers for refinement by centroiding.

## 3. Centroiding

For subvoxel centroiding, we return to the original images and apply a simple low-pass filter by convolving with a three-dimensional Gaussian kernel. The centroiding operation is performed on a region centered on the pixel-accurate location obtained from the previous analysis stage. In dense samples, this operation can suffer from systematic errors depending on the proximity to other particles and the properties of the point-spread function (PSF) of the imaging apparatus. One possible, but computationally expensive, approach to resolve this problem is to try to deconvolve the PSF effects directly and then perform centroiding. We choose an alternative approach, which is to cut off the effects of neighboring particles over distances comparable to the particle size by using a spherical binary mask, with the window size given by the expected particle size. Then, to localize the particles in this subpixel region, we perform a recursive centroiding algorithm, referred to as fracshift in Ref. [55], that consists of repeating the centroiding operation about the new position estimates until the result converges by some criterion. Gao *et al.* [55] showed that this recursive centroiding method is necessary to achieve subvoxel positions without voxel locking. Our implementation follows their algorithm, with some accuracy improvements by the use of a more accurate noncircular areal interpolation in place of the circular shift operation used in the core of the original code to perform multiple passes of the centroiding operator in a local region without reloading regions from memory for every iteration. We find that the majority of particles (>95%) typically converge within 20 iterations. We implement a combination of a global convergence criterion based on a fixed maximum number of iterations for all particles (used for computational convenience to prevent excessive analysis of individual particles), but we allow each particle to perform the required number of iterations until the

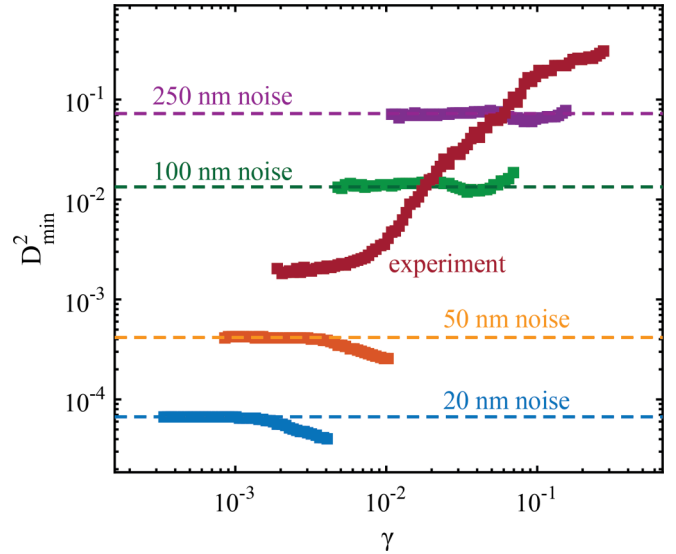


FIG. 9.  $D_{\min}^2$  as a function of strain for four magnitudes of random particle displacements. The experimental noise floor in  $D_{\min}^2$  (red markers) lies between the 50- and 100-nm random displacements, which agrees with the position uncertainty estimate of  $\sim 60$ – $80$  nm from the RMS displacement values.

change in positions is less than a fixed tolerance. This allows the algorithm to converge rapidly for very well-defined peaks and spend more time refining more challenging peaks. We confirm the validity of the subvoxel positions by a number of standard tests, such as computing the distribution of subpixel values in the positions and the noise floor in dynamical quantities.

## APPENDIX B: UNCERTAINTY IN PARTICLE POSITIONS

We make two estimates of the experimental uncertainty in locating particle centers by (1) measuring the root-mean-squared displacement,  $\sigma_{\Delta x} = \sqrt{\langle \Delta x^2 \rangle}$ , in the matrix from  $t$  to  $t + 1$  and (2) adding noise to the positions at  $t = 0$  and measuring the resulting noise floor in  $D_{\min}^2$ .

### 1. RMS displacements

As an upper bound on the uncertainty in particle positions, we measure the root-mean-squared displacement in  $x$ ,  $y$ , and  $z$  in the matrix for each incremental time step  $t$  to  $t + 1$ . The mean value over the duration of the experiment in each dimension is given below.

Dimension	$\sigma_{\Delta x}$ ( $\mu\text{m}$ )	$\sigma_{\Delta x}/D_{\text{part}}$
$x$	0.0589	0.0178
$y$	0.0588	0.0178
$z$	0.0804	0.0244

### 2. Noise floor in $D_{\min}^2$

As a second estimate on the uncertainty in particle positions, we add a displacement of fixed magnitude and random direction to the positions identified at  $t = 0$ . Using



the displaced positions, we calculate  $D_{\min}^2$  according to the procedure outlined in the main text. The noise floors in  $D_{\min}^2$  for displacement magnitudes of 20, 50, 100, and 250 nm are

shown in Fig. 9. The experimental noise floor lies between 50 and 100 nm of random noise, which agrees well with the RMS displacement uncertainty estimate of  $\sim 60\text{--}80$  nm.

- 
- [1] A. Greer, Y. Cheng, and E. Ma, *Mater. Sci. Eng. R* **74**, 71 (2013).
- [2] C. A. Schuh, T. C. Hufnagel, and U. Ramamurty, *Acta Mater.* **55**, 4067 (2007).
- [3] R. Besseling, E. R. Weeks, A. B. Schofield, and W. C. K. Poon, *Phys. Rev. Lett.* **99**, 028301 (2007).
- [4] V. Chikkadi, G. Wegdam, D. Bonn, B. Nienhuis, and P. Schall, *Phys. Rev. Lett.* **107**, 198303 (2011).
- [5] A. Kabla and G. Debrégeas, *Phys. Rev. Lett.* **90**, 258303 (2003).
- [6] M. D. Ediger, C. Angell, and S. R. Nagel, *J. Phys. Chem.* **100**, 13200 (1996).
- [7] P. G. Debenedetti and F. H. Stillinger, *Nature* **410**, 259 (2001).
- [8] C. S. O'Hern, L. E. Silbert, A. J. Liu, and S. R. Nagel, *Phys. Rev. E* **68**, 011306 (2003).
- [9] S. Gokhale, A. Sood, and R. Ganapathy, *Adv. Phys.* **65**, 363 (2016).
- [10] W. L. Johnson and K. Samwer, *Phys. Rev. Lett.* **95**, 195501 (2005).
- [11] Y. H. Liu, C. T. Liu, W. H. Wang, A. Inoue, T. Sakurai, and M. M. Chen, *Phys. Rev. Lett.* **103**, 065504 (2009).
- [12] P. Guan, M. Chen, and T. Egami, *Phys. Rev. Lett.* **104**, 205701 (2010).
- [13] T. Egami, *J. Alloys Compd.* **509**, S82 (2011).
- [14] P. Olsson and S. Teitel, *Phys. Rev. Lett.* **99**, 178001 (2007).
- [15] A. Basu, Y. Xu, T. Still, P. Arratia, Z. Zhang, K. Nordstrom, J. M. Rieser, J. Gollub, D. Durian, and A. Yodh, *Soft Matter* **10**, 3027 (2014).
- [16] V. Chikkadi, D. M. Miedema, M. T. Dang, B. Nienhuis, and P. Schall, *Phys. Rev. Lett.* **113**, 208301 (2014).
- [17] P. K. Jaiswal, I. Procaccia, C. Rainone, and M. Singh, *Phys. Rev. Lett.* **116**, 085501 (2016).
- [18] B. A. Isner and D. J. Lacks, *Phys. Rev. Lett.* **96**, 025506 (2006).
- [19] A. Furukawa, K. Kim, S. Saito, and H. Tanaka, *Phys. Rev. Lett.* **102**, 016001 (2009).
- [20] R. C. Hurley, S. A. Hall, J. E. Andrade, and J. Wright, *Phys. Rev. Lett.* **117**, 098005 (2016).
- [21] J. R. Greer and J. T. M. De Hosson, *Prog. Mater. Sci.* **56**, 654 (2011).
- [22] D. J. Strickland, Y.-R. Huang, D. Lee, and D. S. Gianola, *Proc. Natl. Acad. Sci. USA* **111**, 18167 (2014).
- [23] G. L. Hunter and E. R. Weeks, *Rep. Prog. Phys.* **75**, 066501 (2012).
- [24] J. Crocker, *J. Colloid Interface Sci.* **179**, 298 (1996).
- [25] A. Ikeda, L. Berthier, and P. Sollich, *Phys. Rev. Lett.* **109**, 018301 (2012).
- [26] S. Henderson, T. Mortensen, S. M. Underwood, and W. van Meegen, *Physica A* **233**, 102 (1996).
- [27] E. Bartsch, T. Eckert, C. Pies, and H. Sillescu, *J. Non-Cryst. Solids* **307**, 802 (2002).
- [28] E. R. Weeks, J. C. Crocker, A. C. Levitt, A. Schofield, and D. A. Weitz, *Science* **287**, 627 (2000).
- [29] P. N. Pusey and W. Van Meegen, *Nature* **320**, 340 (1986).
- [30] L. C. Hsiao, S. Jamali, E. Glynos, P. F. Green, R. G. Larson, and M. J. Solomon, *Phys. Rev. Lett.* **119**, 158001 (2017).
- [31] M. H. Cohen and D. Turnbull, *J. Chem. Phys.* **31**, 1164 (1959).
- [32] D. Turnbull and M. H. Cohen, *J. Chem. Phys.* **52**, 3038 (1970).
- [33] F. Spaepen, *Acta Metall.* **25**, 407 (1977).
- [34] A. Argon, *Acta Metall.* **27**, 47 (1979).
- [35] L. Li, E. R. Homer, and C. A. Schuh, *Acta Mater.* **61**, 3347 (2013).
- [36] K. Martens, L. Bocquet, and J.-L. Barrat, *Phys. Rev. Lett.* **106**, 156001 (2011).
- [37] W. L. Johnson, J. Lu, and M. D. Demetriou, *Intermetallics* **10**, 1039 (2002).
- [38] T. Egami, Y. Tong, and W. Dmowski, *Metals* **6**, 22 (2016).
- [39] Y. Suzuki, J. Haimovich, and T. Egami, *Phys. Rev. B* **35**, 2162 (1987).
- [40] A. S. Clarke and H. Jónsson, *Phys. Rev. E* **47**, 3975 (1993).
- [41] T. C. Hufnagel, R. T. Ott, and J. Almer, *Phys. Rev. B* **73**, 064204 (2006).
- [42] W. Dmowski, T. Iwashita, C.-P. Chuang, J. Almer, and T. Egami, *Phys. Rev. Lett.* **105**, 205502 (2010).
- [43] U. K. Vempati, P. K. Valavala, M. L. Falk, J. Almer, and T. C. Hufnagel, *Phys. Rev. B* **85**, 214201 (2012).
- [44] D. Denisov, M. T. Dang, B. Struth, G. Wegdam, and P. Schall, *Sci. Rep.* **3**, 1631 (2013).
- [45] Y. Sun, A. Concustell, and A. L. Greer, *Nat. Rev. Mater.* **1**, 1 (2016).
- [46] Y. Tong, T. Iwashita, W. Dmowski, H. Bei, Y. Yokoyama, and T. Egami, *Acta Mater.* **86**, 240 (2015).
- [47] M. L. Falk and J. S. Langer, *Phys. Rev. E* **57**, 7192 (1998).
- [48] V. Chikkadi, S. Mandal, B. Nienhuis, D. Raabe, F. Varnik, and P. Schall, *Europhys. Lett.* **100**, 56001 (2012).
- [49] E. D. Cubuk, R. Ivancic, S. S. Schoenholz, D. Strickland, A. Basu, Z. Davidson, J. Fontaine, J. L. Hor, Y.-R. Huang, Y. Jiang *et al.*, *Science* **358**, 1033 (2017).
- [50] R. Jana and L. Pastewka, *J. Phys. Materials* **2**, 045006 (2019).
- [51] B. Doliwa and A. Heuer, *Phys. Rev. E* **61**, 6898 (2000).
- [52] K. E. Jensen, D. A. Weitz, and F. Spaepen, *Phys. Rev. E* **90**, 042305 (2014).
- [53] S. Lawrence Marple, *IEEE Trans. Sign. Process.* **47**, 2600 (1999).
- [54] T. Lindeberg, *J. Appl. Stat.* **21**, 225 (1994).
- [55] Y. Gao and M. L. Kilfoil, *Opt. Express* **17**, 4685 (2009).